Feasibility of integrating a very large floating structure with multiple wave energy converters combining oscillating water columns and oscillating flaps

Yong Cheng[a], Fukai Song[a] , Chen Xi[a], Maurizio Collu[b], Zhiming Yuan[a, b], Atilla Incecik[b]

[a]School of naval architecture and ocean engineering, Jiangsu University of Science and Technology, Zhenjiang, 212003, China

[b]Naval Architecture, Ocean and Marine Engineering Department, University of Strathclyde, Glasgow, United Kingdom

Abstract

The installation of wave energy converters (WECs) along the facing-wave side of in-development or pre-existing offshore structures provides an effective cost-sharing solution. In this study, a time-domain numerical model based on the modal expansion theory and the nonlinear potential flow theory, is applied to optimize the size and layout of an in-line array of oscillating water column (OWCs) and oscillating flaps (OFs) deployed along the facing-wave side of a very large floating structure (VLFS). The front/back-wall end of each OWC chamber is hinged by an OF device, and thus the number of OWCs is identical with that of OFs. Comparison with a typical OWC-VLFS integration shows that the addition of OFs can significantly reduce the hydroelastic response of the VLFS. Additionally, wave energy extraction from the design of OFs hinged at the back-wall end of OWCs is enhanced due to more wave energy gathered in the chamber. Under the premise of the same space, the array layout demonstrates both higher conervsion efficiency and hydroelastic reduction. The energy conversion is generally enhanced by increasing the gap, the OWC width, the OF height. The maximum efficiency increases firstly with wave height for weak wave nonlinearity and then decreases for strong wave nonliearity.

Keywords: oscillating water column; oscillating flap; array wave energy converters; very large floating structure; energy conversion efficiency; fluid-structure interaction

1. Introduction

Along with the ongoing spread of the coronavirus disease 2019 (COVID-19), limitation of economic trade activities has led to structural change of world energy consumption. It is summarised from International Energy Agency (IEA) that 2020 demand for oil decreased about 50% in the first quarter compared to the same period in 2019, resulting in an 8% reduction in global CO_2 emissions by 2021 [1]. This is followed by a rapid growth of the demand for renewable energy with a rate of 2.6% every year until 2040 [2]. Wave energy as one of large-reserve renewable energy resoures, is estimated at an allowable exploitation of 29500 TWh every year [3] and provides compensation for the application of wind energy and tidal energy. Nevertheless, to date, wave energy extraction is not fully commercialized due to high levelised cost of electricity (LCOE) with approximately £300/MWh [4]. The competeness of wave power operation need to further be improved by both increasing the energy conversion efficiency and reducing the construction cost of wave energy

---

converters (WECs).

Oscillating water column (OWC) WECs are extensively investigated due to the simple geometric shape and direct working principle which is based on the rising and falling motion of the water in chamber to induce the peneumatic airflow through a turbine [5]. Evans [6] adopted the linear matched function method to obtain the wave energy conversion efficiency of a two-dimensional (2-D) fixed OWC device. In his description, the spatial deformation of water surface in the OWC chamber was not considered in the theoretical model and was assumbed as a finite-width rigid piston. Along the similar technical route, Sarmeto and Falcão [7] analytically studied the dependence of wave energy extraction of a 2-D nearshore OWC on the nonlinear water motion. Subsequently, Ning et al. [8] proposed a dual-chamber cylindrical OWC device and analytically compared the effective frequency bandwith compared with the single chamber OWC, showing that the coupled water oscillation between the inner and outer chambers leads to a wider frequency region. To validate the theoretical findings, Ning et al. [9] conducted relevant model experiments in wave flume and observed different resonant frequencies existing in the sub-chambers. In parallel, the three-dimensional (3-D) numerical model of a dual-chamber stationary OWC is established by Elhanafi et al. [10] using computational fluid dynamics software Star-CCM+. It was concluded that the 3-D scaterring wave effect could cause the reduction of wave energy extraction, especially in short-period waves. He et al. [11] presented a hybrid system which combines an box-type floating breakwater and two individual OWCs installed at its weather side and lee side, respectively. The experimental data illustrated that the combination of the asymmetric chambers i.e. the narrower fore-chamber can enhance the absorption of long-period wave energy. Following this investigation, He et al. [12] examined the spatial non-uniformity of the airflow through the orifices by the averaged wave elevations and obtained the PTO characteristics beforehand. Zhao et al. [13] furthermore expounded the implementation of the triple-chamber OWC device and experimentally compared the hydrodynamic performance to the single- and dual-chamber OWCs. Shalby et al. [14] summarised the developed stages of the multi-chamber OWCs and drawn the commercial-sclae challenges i.e. reliability, robusteness and construction cost.

Above multi-chamber layouts are designed parallel to the wave propagating direction. Another interesting layout is by deploying the in-line array OWCs orthogonal to wave propagation. Howe et al. [15] considered the configuration of an array OWC installed at the fore-end of a floating breakwater and implemented an experimental investigation. It is discovered that the hybrid concept can extracted approximately 80% of the surface wave energy within the tested wave period range. Following this study, Howe et al. [16] studied the wave attenuation and motion performance of the floating breakwater with array OWCs. Zheng et al. [17] developed a mathematical model based on the multi-domain matched method to study the hydrodynamic performance of an array of OWCs placed along a coastal line. This investigation revealed the constructive array effect occurring at a certain renge of wave periods. Doyle and Aggidis [18] concerned the comparison of an array of OWCs with separated PTO systems and a shared PTO system, showing that the spacing distance affect significantly the output power of the array OWC. Han and Wang [19] developed a hybrid numerical-analytical method in which the internal domain problem is solved by using matched eigenfunctions whereas the external domain problem is solved by using boundary element method (BEM), to investigate the wave absorption by a breakwater with array OWC system. Zheng and Zhang [20] proposed a hybrid-type WEC system consisting of an offshore OWC device and array OB hinged around it, and compared the hydrodynamic responses with an isolated OWC and isolated

array of OBs. Cui et al. [21] theoretically examined the hydrodynamic performance of an OWC-OB hybrid WEC system, focusing on the extracted energy comparsion of OWC and OB devices. The conclusion supports the viewpoint by Zheng and Zhang [20], indicating that the energy extraction by the OWC is higher than that by the OB in long-period waves and vice versa in short-period waves. In order to reduce the wave loads on the body surface, Wang et al. [22] proposed a pitching flap instead of the fixed lip-wall installed at the front side of a dual-chamber OWC. It is demonstrated that the pitching flap with enough small constrained stiffness can broaden the frequency bandwidth of the energy efficiency curve.

With the marine industries advancing from shallow to deep water, floating offshore multi-purpose structures are proposed to utilize ocean space and exploit marine resources. Integration of array hybrid-type WECs with a VLFS can accomplish the cost-sharing, the space-sharing and the function-sharing strategy, which provides a viable solution to extract available wave energy and simultaneously to create land from sea. In addition to their respective functions, the deployment of WECs at the weather side of the VLFS can reduce the motion response of the VLFS by attenuating transmitted wave height and the multi-modal scattering waves generated by VLFS in turn boost wave energy absorption of WECs, which produces the synergistic effect between WECs and VLFS. Mustapa et al. [23] discussed the benefits brought by the integration of WECs and large marine structures in detail. Nguyen et al. [24] presented an array of raft-type WECs installed at the fore edge of a VLFS, and applied numerical model to predict the hydrodynamic performance of the integrated system. It is found that the installation of WECs not only extact incident wave energy, but also reduce the hydroelastic response of the VLFS. Later, Nguyen et al. [25] proposed heaving-mode WECs attached to the edge of the VLFS at one end and to the seabed at the other end, showing that the heaving WECs would be more suitable in long-period waves with maximum conversion efficiency of 0.6. Zhang et al. [26] designed an embedded WEC installed in between floating modules, which absorbs the relative pitching motion between adjacent modules. Zhang et al. [27] further used the Hooke Jeeves method to determine the optimal balance of the PTO damping between the energy extraction and motion suppression. A discrete-module-beam-bending hydroelastic method was also used to analyze the effects of hinged location and stiffness on wave energy extraction of a VLFS with a WEC unit by Zhang et al. [28]. Tay [29] numerically investigated the wave energy extraction of arrary WEC integrated with a long-length floating breakwater, focusing on the effects of mooring stiffness, wave period and wave direction. Crema [30] conducted experimental investigation of multiple in-line OWCs integrated at the fore-end of a semi-sumbersible large floating platform. Float Inc. [31] described an offshore floating port with Rho-Cee WECs which combines three OWC chambers with different widths. Similar to multi-chamber OWC WECs, the integrated system can extract wave energy for a wide range of wave periods due to the coupled resonance among chambers. Sheng et al. [32] utilized experimental tests to investigate the energy output performance of four eagle-shape buoys attached at the edges of a moored floating platform. Cheng et al. [33] performed a 3-D numerical simulation of an array of heaving WECs as modular breakwaters integrated at the weather side of a VLFS using nonlinear potential flow theory combined with the Mindlin plate theory.

Above mentioned researches mainly concentrate on the hydrodynamic performance of the isolated multi-chamber or array OWC devices, the integration of OWCs and a VLFS, and the integration of OBs and a VLFS. However, the relating works on the hybrid OWC-OB WEC system integrated with a VLFS are still scarce, especially for 3-D nonlinear numerical simulations.

Moreover, the fluid-structure interaction is more complex compared with single-mode WECs due to the mutual coupled effects among the internal water motion in chamber, the OB rigid motions and the multi-modal hydroelastic motion of the VLFS. Therefore, the motivation and novelty of this paper is twofold; firstly to consider the combination of array oscillating flap (OF)-type WECs and OWCs which are integrated at the fore-end of a VLFS, and secondly to develop a 3-D time-domain nonlinear model to discuss the effect of the installed location of flaps, the number of WECs, WEC geometric parameters and wave parameters on both the wave energy extraction and the hydroelastic response. This will help boost commercial-scale application of WECs, which simultaneously achieves the utilization of ocean space and exploitation of marine energy. This paper is arranged as follows. Section 2 describes the establishment of the multi-body hydroelastic model based on nonlinear modal expansion method in the time-domain. The corresponding convergence tests and validations for the developed model are given in Section 3. Then, in Section 4, the optimal size and configuration of WECs are obtained by conducting parametric studies. Finally, the conclusions are summarized in Section 5.

2. Mathematical model

2.1 water motion equations

A sketch of a hybrid WEC-VLFS system is shown in Fig. 1. The WEC devices are composed of a number (N) of OWCs and OFs hinged at the wall end of each OWC. Here, $N=2$ is set as an example. The array layout is orthogonal to incident wave direction. The geometric dimension is identical for all OWC chambers and its width, length, front-wall draft, back-wall draft and wall thickness are represented by b_o, l_o, d_{o1}, d_{o2} and s_o respectively. The submerged height of each flap is denoted by d_f, while the length and thickness are the same with those of the OWC chamber. There are two-type PTO systems which are a pneumatic PTO system for the OWC device and a hydraulic PTO system for the flap device, respectively. The whole WEC integration with an in-line array layout which is orthogonal to incident wave direction, is placed at the upstream distance b_g from a pontoon-type VLFS with dimensions of length l_v×width b_v×draft d_v. Thus, these WEC devices can extract adequately wave energy and simultaneously reduce the hydroelastic response of the VLFS as attenuating wave devices. In order to accurately simulate the multi-body hydrodynamic problem, two right-hand Cartesian coordinate systems are defined. A space-given coordinate system $o_0x_0y_0z_0$ is used to describe the wave field, and three body-given coordinate systems i.e. VLFS-given $o_vx_vy_vz_v$, and flap-given $o_fx_fy_fz_f$ are used to describe the motion responses of floating bodies. Based on the potential flow theory, the motion characteristic of the inviscid, irrotational and incompressible fluid is denoted by a velocity potential Φ which satisfies the Laplace govering equation and the following boundary condition on free surface

$$\begin{cases} \dfrac{\mathrm{d}\vec{r}}{\mathrm{d}t} = \dfrac{\partial \Phi}{\partial \vec{r}} - v\vec{r} \\[2mm] \dfrac{\mathrm{d}\Phi}{\mathrm{d}t} = \dfrac{1}{2}\left|\nabla\Phi\right|^2 - g\eta - \dfrac{P_a}{\rho_w} - v\Phi \end{cases} \qquad \text{on } S_{Fo} \text{ and } S_{Fi} \qquad (1)$$

where S_{Fo} and S_{Fi} denote the free surfaces outside and inside of the OWC chamber, respectively; ρ_w is the water density; η is the wave elevation; g is the gravity acceleration, respectively; $\vec{r}$ represents the location vector of water particles; P_a is the air pressure above S_{Fo} or S_{Fi}.

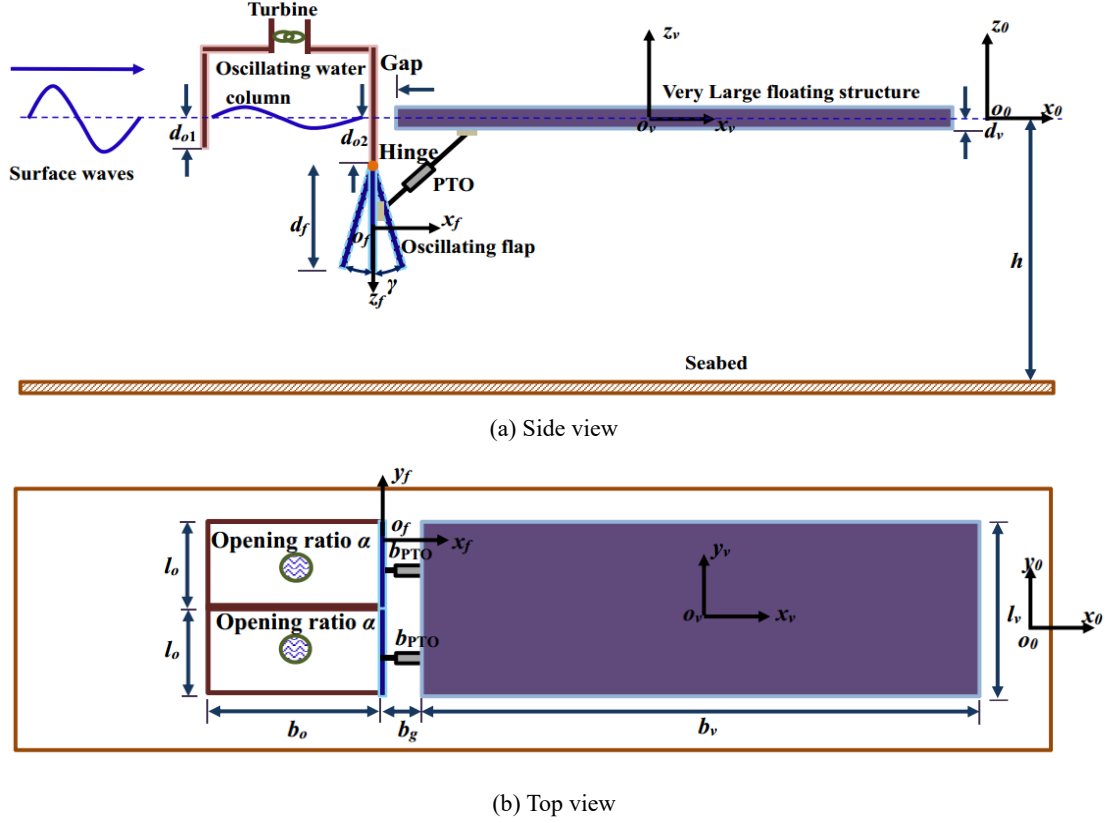(a) Side view

(b) Top view

Fig. 1. A diagram of general layout of an array of OWCs and OFs deployed at the facing-wave side of a VLFS

The instantaneous motion conditions on VLFS and flaps can be expressed as

$$\frac{\partial \Phi}{\partial n} = \dot{\gamma}_i \cdot (x n_y - y n_x) \qquad \text{on } S_f \qquad (2)$$

$$\frac{\partial \Phi}{\partial n} = \dot{w} \cdot n_z \qquad \text{on } S_v \qquad (3)$$

where S_f and S_v denote the body surfaces of the flap and the VLFS, respectively; (n_x, n_y, n_z) denotes the unit normal vector; γ_i denotes the angle displacement of the i-th oscillating flap; w represents the hydroelastic response of the VLFS, and is written as the modal expansion form

$$w(x, y, t) = \left\{ f^w \right\}^T \left\{ \zeta \right\} \qquad (4)$$

where ζ and f^w are the modal amplitude and function; superscript T denotes matrix transposition.

The boundary conditions on other wall surfaces i.e. seabed and OWC are set as impermeable conditions. Additionally, the following fifth-order incident wave potential Φ_I and elevation η_I are defined as the initial condition in the time-marching simulation.

$$\Phi_I = \frac{\omega}{k^2} \sum_{i=1}^{5} \delta_i \cosh(ik(z+h)) \cdot \sin\left[i(kx - \omega t + \theta_0) \right] \qquad (5)$$

$$\eta_I = \frac{1}{k} \sum_{i=1}^{5} \varepsilon_i \cos\left[i(kx - \omega t + \theta_0) \right] \qquad (6)$$

where ω is the angle frequency; k is wave number; θ_0 is the random phase; h is the water depth; δ_i and ε_i are wave coefficients defined in Ref. [34].

The above boundary value problems can be transformed the integral equation by using the Green

function G

$$\chi(p_s)\Phi(p_s) = \iint_S G(p_s,q_f)\frac{\partial\Phi(q_f)}{\partial n} - \Phi(q_f)\frac{\partial G(p_s,q_f)}{\partial n}\,ds \tag{7}$$

where χ is the solid angle coefficient; S denotes the whole domain boundary; $p_s=(x_s, y_s, z_s)$ and $q_f=(x_f, y_f, z_f)$ denote source point and field point, respectively.

Eq. (7) can be solved by applying the boundary element method (BEM). After obtaining the velocity potential, the hydrodynamic loads on the VLFS and the OFs can be calculated based on the Bernoulli pressure integration

$$F_v = \iint_{S_v} -\rho_w\left\{\frac{\partial\Phi}{\partial t} + \frac{1}{2}|\nabla\Phi|^2 + gz\right\}\cdot n_z ds \ , \tag{8}$$

$$M_i = -\rho_w\iint_{S_f}(\frac{\partial\Phi}{\partial t} + \frac{1}{2}|\nabla\Phi|^2 + gz)\cdot(xn_z - zn_x)dS \tag{9}$$

where F_v is the vertical force on the VLFS; M_i is the fluid moment on the i-th oscillating flap. The calculation of the first term in Eqs. (8) and (9) is related to the node location at different times. In the linear hydrodynamic problem, this term can be straightforwardly calculated using backward finite difference scheme because all boundary conditions are assumed to statisfy on the equilibrium location i.e. the calm water surface. However, in the fully nonlinear problem, the nodes on the water surfaces and wetted body surfaces moves with time, which easily leads to the numerical divergence and the inaccurate values. To avoid this problem, the auxiliary function method is applied in this paper to indirectly calculate the time derivative of the velocity potential, and thus Eqs. (8) and (9) can be transformed into

$$F_v = -\rho_w\ddot{w}\iint_{S_v}\psi_1\cdot n_z dS - \rho_w\iint_{S_v}\left(\psi_2 + \frac{1}{2}|\nabla\Phi|^2 + gz\right)\cdot n_z dS \tag{10}$$

$$M_i = -\rho_w\ddot{\gamma}\iint_{S_f}\psi_3\cdot(xn_z - zn_x)dS - \rho_w\iint_{S_f}(\psi_4 + \frac{1}{2}|\nabla\Phi|^2 + gz)\cdot(xn_z - zn_x)dS \tag{11}$$

where ψ_i (i=1 to 4) is the auxiliary function which is solved by using the same procedure with velocity potential.

2.2 Structural motion equations

Based on the Newton's second law and the Mindlin thick plate theory, the motion equations of the rigid floating bodies i.e. the OFs and the flexible floating bodies i.e. the VLFS can be expressed

$$I_i\ddot{\gamma}_i + b_{pto}\dot{\gamma}_i = M_i \tag{12}$$

$$\iint_{S_v} D(\boldsymbol{B_1} + \boldsymbol{B_2})\{w\} + \rho_s\omega^2\boldsymbol{B_3}\{w\}ds = \{F_v\} \tag{13}$$

where I_i is the rotational inertia of the i-th flap; b_{pto} denotes the PTO damping coefficient; D is the bending rigidity; ρ_s denotes the structural density; B_i(i=1, 2, 3) denotes the constant matrix.

The hydroelastic motion equation i.e. Eq. (13) of the VLFS is solved by the finite element method (FEM) which discretizes the VLFS into a finite number of the Mindlin plate elements. The

stiffness and mass matrixes of each element is derived from the Hamiltonian energy principle combined with basis shape functions. These discrtised matrixes are then assembled to establish the global motion equation for the entire VLFS model as

$$[M]\{\ddot{w}\}+([K_f]+[K_s]+[K_{re}])\{w\}=\{F_v\} \tag{14}$$

where $[M]$ is the global mass matrix; $[K_f]$, $[K_s]$ and $[K_{re}]$ are the global flexural stiffness matrix, the global shear stiffness matrix and the global restoring force matrix, respectively. All these matrixes can be written as

$$[M]=\sum_e\iint_e\rho_s[N]^T\begin{bmatrix}h_v & 0 & 0\\ 0 & h_v^3/12 & 0\\ 0 & 0 & h_v^3/12\end{bmatrix}[N]ds_e\,, \tag{15}$$

$$[K_f]=\sum_e\iint_e[B_f]^T[D_f][B_f]ds_e\,, \tag{16}$$

$$[K_s]=\sum_e\iint_e[B_s]^T[D_s][B_s]ds_e\,, \tag{17}$$

$$[K_{re}]=\sum_e\rho_w g\iint_e[N]^T\begin{bmatrix}1 & 0 & 0\\ 0 & 0 & 0\\ 0 & 0 & 0\end{bmatrix}[N]ds_e\,, \tag{18}$$

where D_f denotes the flexural elasticity matrix; D_s denotes the shear elasticity matrix; $[N]$ is the shape function matrix; e means integration on the single element; $[B_f]$ is the flexural strain-displacement matrix; $[B_s]$ is the shear strain-displacement matrix.

Eq. (14) can further be wirtten in the following form by combining with Eq. (4) and premultiplying the modal function vector $\{f^w\}$

$$\{f^w\}[M]\{f^w\}^T\{\ddot{\zeta}\}+\{f^w\}([K_f]+[K_s]+[K_{re}])\{f^w\}^T\{\zeta\}=\{f^w\}\{F_w\} \tag{19}$$

Eqs. (12) and (19) are solved by the fourth order Runge-Kutta method. The rotational angle of the oscillating flaps can be directly obtained from solving Eq. (12). The solved modal amplitudes from Eq. (19) are back-substituted into Eq. (4) to obtain the hydroelastic responses of the VLFS.

2.3 Wave energy extraction and hydroelastic reduction

After the water surface characteristics in the OWC chamber are obtained from Eq. (7), the pneumatic pressure P_a^i for the i-th OWC chamber can be written

$$P_a^i=\frac{\rho_a}{2}\left(\frac{1}{\alpha C_c}-1\right)^2\left|\frac{d\eta}{dt}\right|\frac{d\eta}{dt} \tag{20}$$

where ρ_a is the air density; C_c is the contraction coefficient determined by the Chisholm expression [35]

$$C_c=\frac{1}{0.639(1-\alpha)^{0.5}+1} \tag{21}$$

where C_c is the opening area ratio which is defined as the ratio of the horizontal cross-sectional areas of the orifice and the OWC chamber.

The period-average pneumatic energy $E^i_{p(OWC)}$ in the i-th OWC chamber can be calculated as

$$E^i_{p(OWC)} = \frac{A^i_c}{mT} \int_t^{t+mT} P^i_a \frac{d\eta}{dt} dt \tag{22}$$

where A_c^i is the cross-section area of the water surface in the i-th OWC chamber; m is the number of wave period.

The period-average generated power $E^i_{P(\text{flap})}$ from the rotation of the i-th OF, is calculated

$$E^i_{P(flap)} = \frac{b_{pto}}{mT} \int_t^{t+mT} \dot{\gamma}_i^2 dt \tag{23}$$

The incident wave energy per unit wave front can be obtained based on the input mechanism of wave energy flux

$$E_w = \frac{1}{8} \rho_w g H_i^2 c_g \tag{24}$$

where c_g is the moving velocity of wave group, and is calculated by

$$c_g = \frac{\omega}{2k} \left(1 + \frac{2kh}{\sinh 2kh} \right) \tag{25}$$

The energy conversion efficiency of the OWC and OF can be given, respectively as

$$R_1 = \frac{\sum_{i=1}^{K} E^i_{p(OWC)}}{E_w \cdot l_v} \tag{26}$$

$$R_2 = \frac{\sum_{i=1}^{K} E^i_{p(flap)}}{E_w \cdot l_v} \tag{27}$$

Thus, the overall conversion efficiency of the WEC system is written as:

$$R = R_1 + R_2 \tag{28}$$

The hydroelastic reduction H_r of the VLFS due to the installation of the WEC system can be defined as

$$H_r = 1 - \frac{w_0}{w_1} \tag{29}$$

where w_0 and w_1 denote the response amplitude of the VLFS with and without the WEC sytem, respectively.

3. Validation

3.1 Convergent tests

An array OWC-OF WEC system integrated in the fore-end of a pontoon-type VLFS is selected to conducted the mesh and temporal convergent tests. The number of WECs i.e. OWCs and OFs is considered as $N=2$ which means $l_o/b_v = l_f/b_v = 1/2$. The non-dimensional length, width and draft of the VLFS are $l_v/h = 2.17$, $b_v/h = 0.43$, $d_v/h = 0.026$, in which the water depth is set as $h = 2.3$ m. The front

wall draft, the back wall draft, the chamber width and the wall thickness of the OWC are d_{o1}/h=0.009, d_{o2}/h=0.022, b_o/h=0.11 and s_o/h=0.01, respectively. The OF has a submerged depth of d_f/h=0.065. The WEC-VLFS gap distance is set as b_g=0. The PTO damping coefficients for the OWC and OF devices are set as α=1.2% and b_{pto}=3.0 N•m•s/radian, respectively. Three mesh schemes are examined on boundary surfaces of the comupational domain, i.e. Mesh a (15 segments per wavelength), Mesh b (30 segments per wavelength) and Mesh c (7 segments per wavelength). The time step for three mesh schemes is defined as dt=T/60 after completing the temporal convergence. Fig. 2(a) and (b) show the time series of the wave elevation in the OWC chamber and the rotational acceleration of the OF for period T=1.1 s and wave height H_i=0.02 m. For water motion in the chamber as shown in Fig. 2(a), the phase difference between Mesh a and Mesh c is larger than 5% even though the amplitude difference is less than 5%. The difference in the crests and troughs of the rotational accleration in Fig. 2(b) is larger than 7% between Mesh a and Mech c. The numerical solutions obtained from Mesh a match well with those from Mesh b, with both amplitude and phase differences less than 5%. Fig. 3 shows the comparsion of the vertical deflection amplitude along the the longitudinal centreline among different mesh schemes. The hydroelastic response of the VLFS converges rapidly with increasing mesh number, and only slight difference between Mesh a and Mesh b is observed in figure. It can be concluded that Mesh a and time step dt=T/60 are converged sufficiently, and are used in the following parametric analysis.
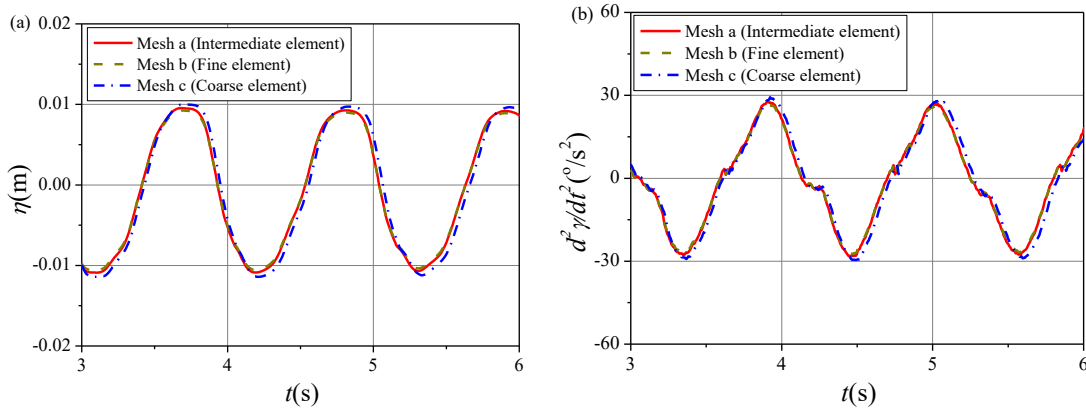

Fig. 2. Convergence of (a) the wave elevation in the OWC chamber and (b) the rotational acceleration of OFs with different meshe schemes
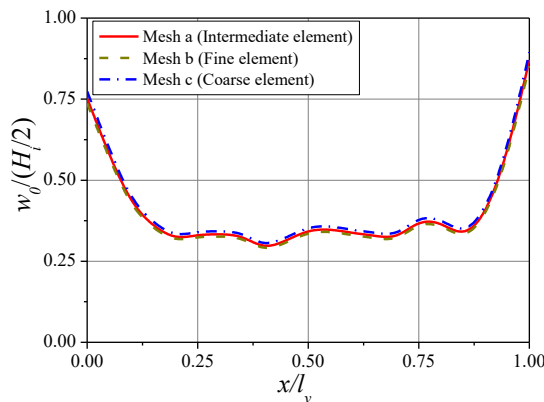

Fig. 3. Convergence of the hydroelastic response of the VLFS with different meshe schemes

3.2 OWC

The present numerical model is used to solve the hydrodynamic performance of a triple-chamber OWC device described by Zhao et al. [13]. The experimental water depth is h=0.6 m. The length,

width and draft of the OWC are l_o=0.78 m, b_o=0.64 m and d_o=0.2 m, respectively. The ratio of each chamber widths is 1:1:1, and the opening ratio of α=1.0% is adopted. Fig. 4 shows the numerical and experimental comparison of the overall energy conversion efficiency R. It can be obtain from this figure that the general shapes of the conversion efficiency curves correlate well with each other, although the numerical values is slightly over-predicted due to the energy dissipation induced by the viscous fluid. In addition, the twin-peak phenomenon which is due to the existence of mulptiple resonant frequencies corresponding to each chamber, is accurately captured by the numerical model. Fig. 5(a) and (b) further display the variation of the reflection coefficient and the transmission coefficient with dimensionless wave number kh, respectively. The good agreement between numerical and experimental results is observed in these figures. The numerical over-prediction is only observed for the transmission coefficient but has weak influence on the reflection coefficient, which indicates that the viscous effect plays a more important role in the transmission waves comapared to the reflected waves.
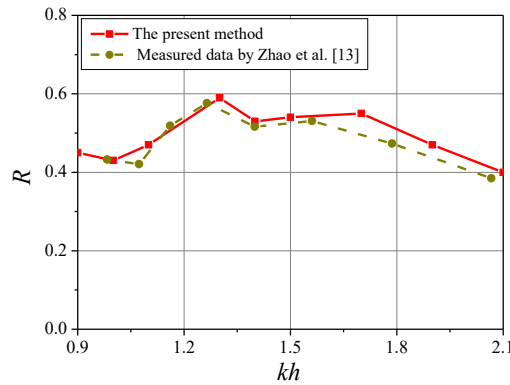
Fig. 4. Comparison of the energy conversion efficiency obtained from the present method and the experimental results in Zhao et al. [13]
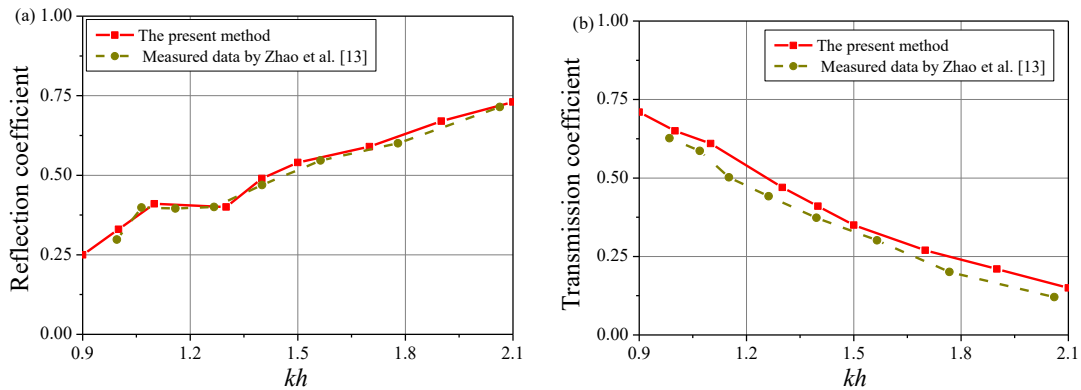

Fig. 5. Comparison of (a) the reflection coefficient and (b) the transmission coefficient obtained from the present method and the experimental results in Zhao et al. [13]

3.3 Osillating flap

The present model is then applied for the simulation of an OF interacting with regular waves. The flap is hinged at 0.16 m from the seabed, and its geometric parameters is height d_f=0.48 m, l_o=1.04 m and moment of inertia I_f=1.84 kgm². The corresponding experiments have been conducted by Wei et al. [36]. The static water depth is set as 0.691 m. Fig. 6 shows the time series of the rotational angle of the flap for period T=2 s and wave height H_i=0.12 m. The CFD solutions obtained by Wang and Liu [37] are also given in figure. The experimental data can be reproduced well by the

developed numerical model. Fig. 7(a) and (b) further display the time series of the wave elevation at the upstream distance 0.9 m and downstream distance 0.9 m from the flap, respectively. It can be seen that the elevation curves give distinct nonlinear characteristics of higher-order waves due to intetratcion between the flap and the water. The variation trend with time agrees satisfactorily among the present numerical model, the experimental data and the CFD model.
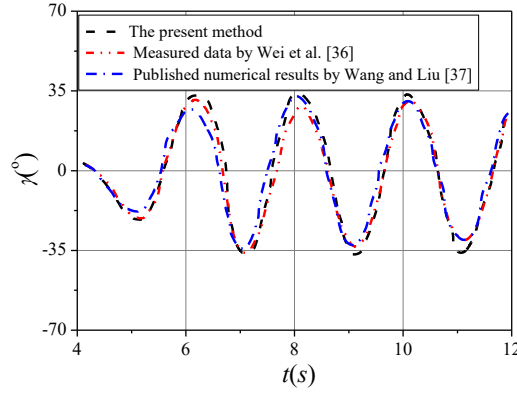

Fig. 6. Comparison of the rotational displacement obtained from the present method, the experimental results in Wei et al. [36] and the published CFD results in Wang and Liu [37]
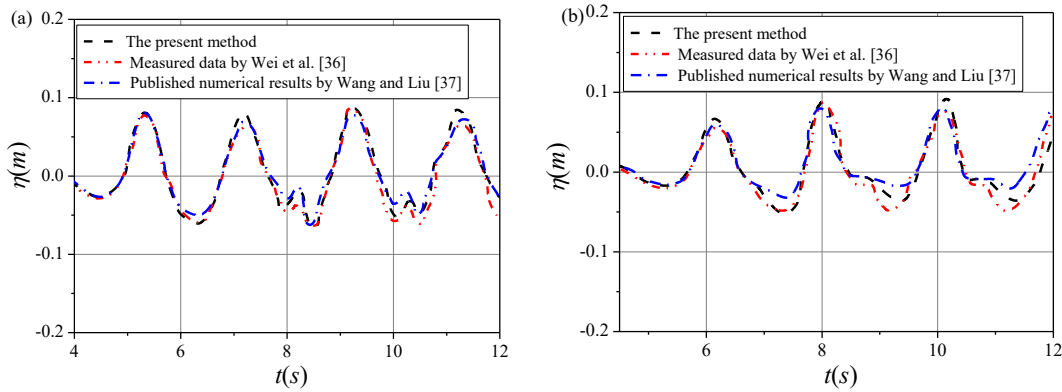
Fig. 7. Comparison of (a) the upstream wave elevation and the downstream wave elevation obtained from the present method, the experimental results in Wei et al. [36] and the published CFD results in Wang and Liu [37]

3.4 VLFS

The developed hydroelastic model is validated by comparing with a experimental example of a pontoon-type VLFS described by Yago and Endo [38]. The key input parameters of this case are listed in Table 1. Fig. 8(a) and (b) shows the distribution of the maximum hydroelastic deflection along the longitudinal centerline for tested wavelength λ=2 m and 6 m. The numerical results of Nguyen et al. [25] are also plotted in figures. It can be observed that the numerical results by the present method agree well with the experimental data obtained from Yago and Endo [38] and the published numerical results obtained from Nguyen et al. [25]. Additionally, the similar distributed trends demonstate that the deflection degeree of the VLFS in short-period waves as shown in Fig. 8(a) is more obvious than that in long-period waves as shown in Fig. 8(b).
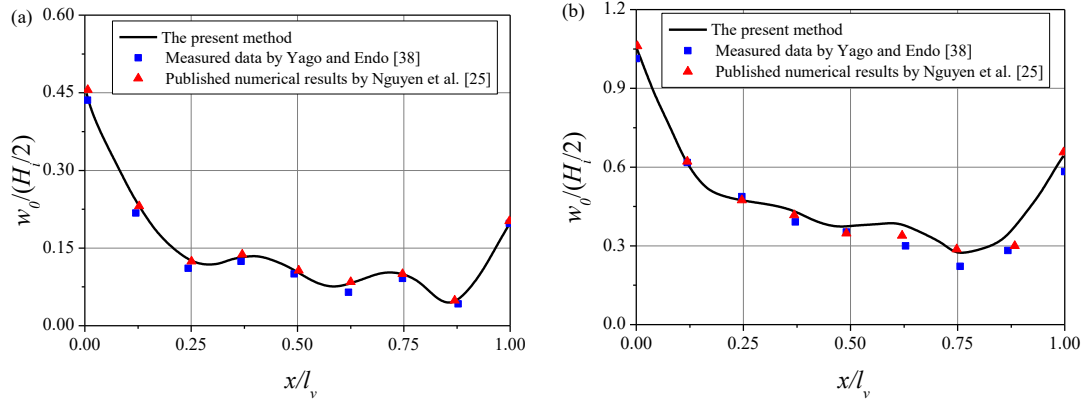
Fig. 8. Comparison of the vertical deflection obtained from the present method, the experimental results in Yago and Endo [38] and the exsiting numerical results in Nguyen et al. [25]

4. Results and discussions

The performance comparison between the typical OWC-VLFS integration and the present OWC-OF-VLFS integration with different OF locations is firstly conducted in this section. Then, the effects of the WEC-VLFS gap, the submerged depth of the OF, on the hydrodynamics of the WEC-VLFS integration are studied. The main objective is to provide guidance for the optimized design of the hybrid OWC-OF WEC system with higher wave energy conversion and hydroelastic reduction.

4.1 Comparison with a typical OWC-VLFS integration

In this sub-section, the hydrodynamic characteristics of the OWC-OF-VLFS integration are compared with a typical OWC-VLFS integration in terms of wave energy conversion efficiency, hydroelastic response and hydroelastic reduction. Here, the single flap and single OWC chamber are considered, as shown in Fig. 9. The typical OWC-VLFS is named as Case 1, as shown in Fig. 8(a). For the OWC-OF-VLFS integration, two different OF layouts are performed i.e. the OF installed at the front-wall end of the OWC as shown in Fig. 9(b) and the OF installed at the back wall end of the OWC as shown in Fig. 9(c), which are named as Case 2 and Case 3. Both the OWC chamber length and the flap length are equal to the VLFS width i.e. $l_o/h = l_f/h = b_v/h = 0.43$. Here, water depth is $h=2.3$ and other physical dimensions are kept the same with those in Section 3.1.
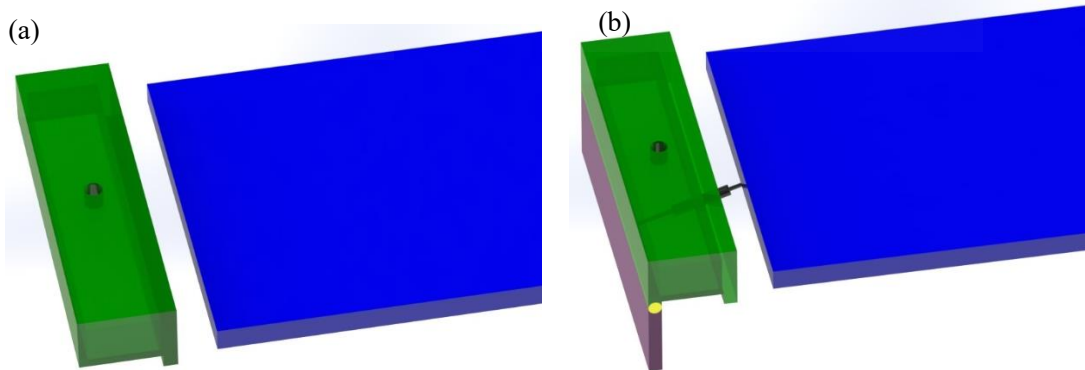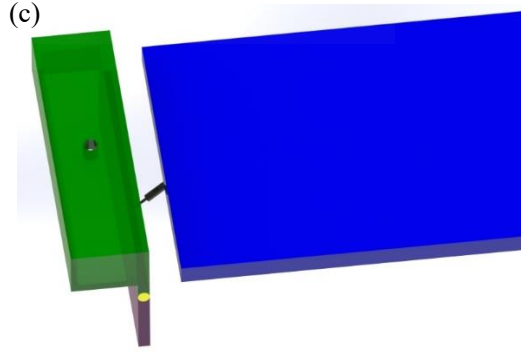
Fig. 9. Schematic diagrams of (a) Case 1, (b) Case 2 and (c) Case 3

Fig. 10 shows the comparison of the overall energy conversion efficiency by the OWC-VLFS integration and the OWC-OF-VLFS integration for wave height H_i=0.02 m. It can be seen that the overall efficiency for Case 2 is apparently less than that for Case 1 in short-period waves with a maximum reduction ratio of 30.4%. This is because that although the OF device can extract part of wave energy, short waves are easily reflected by the OWC when the OF is hinged at the front wall of the OWC and cannot be transmitted into the chamber. However, it is completely opposite for the comparison of Cases 3 and 1 with a maximum increased ratio of 27.2% due to the high reflection ability of the back wall of the OWC. Waves that enter into the OWC chamber can be further reflected by the flap wall installed on the back wall of the OWC. In extreme long-period waves, the wave extraction ability is almost same for the three integrations, which is due to the finite plate thickness of the OF. This implies that the effective frequency bandwith around short-period waves is broadened by the OWC-OF integration Case 3 compared with the OWC-only Case 1, but is unchanged around long-period waves.

Additionally, it is worth mentioning that the variation of the conversion efficiency is associated with two resonant modes which are determined by the OWC and OF devices, respectively. In this particular single-chamber case, these resonant periods are $T_f(g/h)^{1/2}$=1.1 and $T_f(g/h)^{1/2}$=1.79 which are calculated by

$$T_f = 2\pi / \sqrt{\frac{(I + a_z)}{C_z}} \tag{30}$$

$$T_o = 2\pi / \sqrt{\frac{g}{(d_o + 0.41\sqrt{A_c^i})}} \tag{31}$$

where a_z is the added mass of the OF; C_z is the restoring stiffness. This suggests that the occurring period of the maxium efficiency is basically unaffected by the addition of the OF, and is mainly dominated by the resonant period of the OWC.
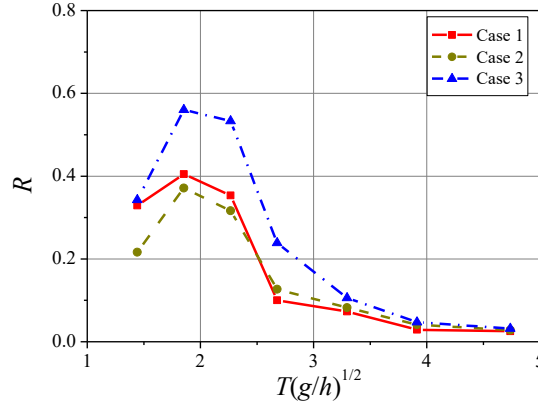
Fig. 10. Variations of energy conversion efficiency R with dimensionless wave period $T(g/H_l)^{1/2}$ for different designs

Fig. 11(a) and (b) shows the dimensionless hydroelastic response amplitude $w_0/(H_i/2)$ along the longitudinal centreline for $T(g/h)^{1/2}$=1.8 and 4.7, respectively. In order to illustrate the hydroelastic reduction of the WEC devices, the results obtained from the isolated VLFS are also given in figures. It can be seen that the hydroelastic response of the hybrid WEC-VLFS system is generally less than that of the single VLFS in both short- and long-period waves. The hydroelastic reduction is further enhanced by the addition of the OF in short-period waves as shown in Fig. 11(a), but the differences in $w_0/(H_i/2)$ of three designs are slight in long-period waves as shown in Fig. 11(b). This behaviour can be explained that short-period waves with low transmission are easily reflected by the OF, while long-period waves propagate into the OWC chamber to be attenuated by the water motion in the chamber.
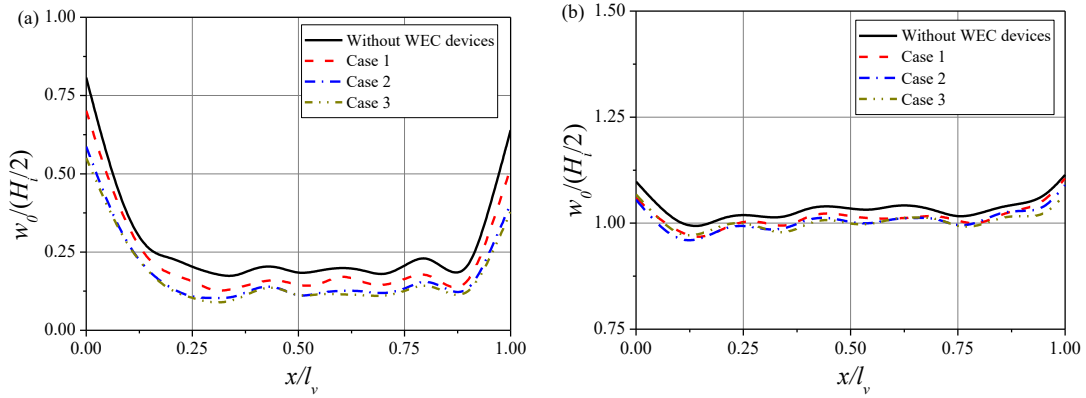

Fig. 11. Distributions of dimensionless vertical deflection amplitude $w_0/(H_I/2)$ along longitudinal centreline for (a) $T(g/h)^{1/2}$=1.8 and (b) $T(g/h)^{1/2}$=4.7

Fig. 12 displays the hydroelastic reduction at the fore-end of the VLFS for all simulated wave periods. It can be found that the hydroelastic reduction decreases with increasing wave period for all cases, and the maximum reduction occurs at the smallest wave period $T(g/h)^{1/2}$=1.4 with H_r= 0.7 for the OWC-OF-VLFS integration and H_r= 0.52 for the OWC-VLFS integration. It is remarkable that the hydroelastic reduction for Case 3 is the largest in the period region 1.8< $T(g/h)^{1/2}$<3.3, which is because the height and the overall masss of the water column in the WEC-VLFS gap increases when the OF is installed at the back wall of the OWC. Nevertheless, both types of the OWC-OF-VLFS integration demonstrate a better performance in reducing the hydroelastic response when compared to an equivalent OWC-VLFS integration in short-period waves. The hydroleastic reduction for three designs is almost identical in long-period waves i.e. $T(g/h)^{1/2}$=4.7. This indicates

that the hydroleastic reduction of the VLFS is simultaneously controlled by the OWC and OF devices, but is mainly dominated by the OWC in long-period waves.
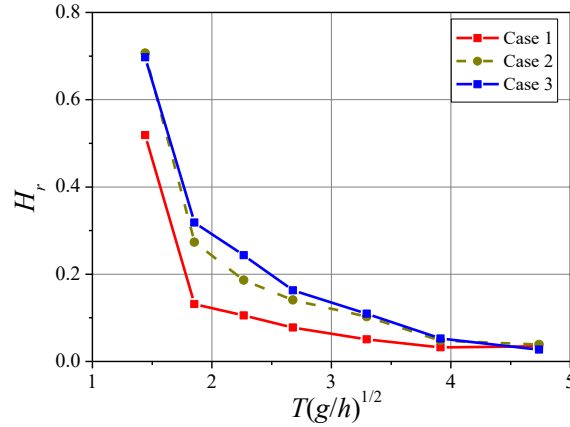

Fig. 12. Variations of hydroelastic reduction H_r with dimensionless wave period $T(g/H_l)^{1/2}$ for different designs

4.2 Effect of different array WEC layouts

The layout of the array OWC-OF WEC system is determined according to the VLFS width. In this section, three examples of three different WEC numbers (i.e. N=1, 2 and 3) which correspond to the geometrical dimensions l_o/b_v =l_f/b_v=1, l_o/b_v =l_f/b_v=1/2 and l_o/b_v =l_f/b_v=1/3, respectively. The OF is located at the back-wall end of the OWC and other parameters are maintained the same with Fig. 12. Fig. 13(a)-(c) display the distribution of the energy conversion efficiency of the OWC, the OF and the overall system with wave period for different array layouts. It can be seen that, from the perspective of the maximum conversion efficiency, the performance of each OWC device among the array layouts is better than that of single isolated VLFS-integrated OWC device. However, this is completely oppositive for the OF devices. As shown in Fig. 13(a), the performance improvement of the OWC with smaller dimensions and more numbers mainly occurs around the resonant period which is almost unchanged by the OWC numbers. This reason is that the water mass in each chamber decreases with increasing the OWC number, leading to violent motion of the internal water, which in turn enhance wave energy extraction. Fig. 13(b) indicates that the energy conversion decreases with increasing OF number for most of wave periods considered in this paper. This is associated with the fact that the wave force on each OF surface decreases with increasing OF number due to the reduction of the effective seaward area of each OF, resulting in smaller rotational displacement as shown in Fig. 14. Moreover, the resonant period of the OF shifts to a longer period, which is inconsistent with the intuitive understanding that the occurring period of the maximum conversion efficiency is identical with that of the maximum displacement. Actually, the conversion efficiency is propotional to the period-average generated power and is inversely proportional to the incident wave power, as indicated in Eq. (25). On the other hand, the incident wave power increases with increasing wave period. Consequently, the period corresponding to the maximum efficiency is dependent on both the wave period and the resonant period of the body motion. By comparing Fig. 13(a) and (b), it is clear that the effeiciency of the OWC is superior to that of the OF, especially for short-period waves. This is because that short-period wave energy is concentrated on the water surface with the range of a wave height, and rapidly diminishes along water depth. In this particular case, the submerged location of the OF is smaller than the wave height, and hence does not contribute much the overall energy conversion efficiency. In Fig. 13(c), the maximum overall

efficiencies are $R=0.56$, 0.69 and 0.70 for $l_o/b_v = l_f/b_v=1$, $l_o/b_v = l_f/b_v=1/2$ and $l_o/b_v = l_f/b_v=1/3$, respectively, which are almost in accordance with those of the OWC devices.
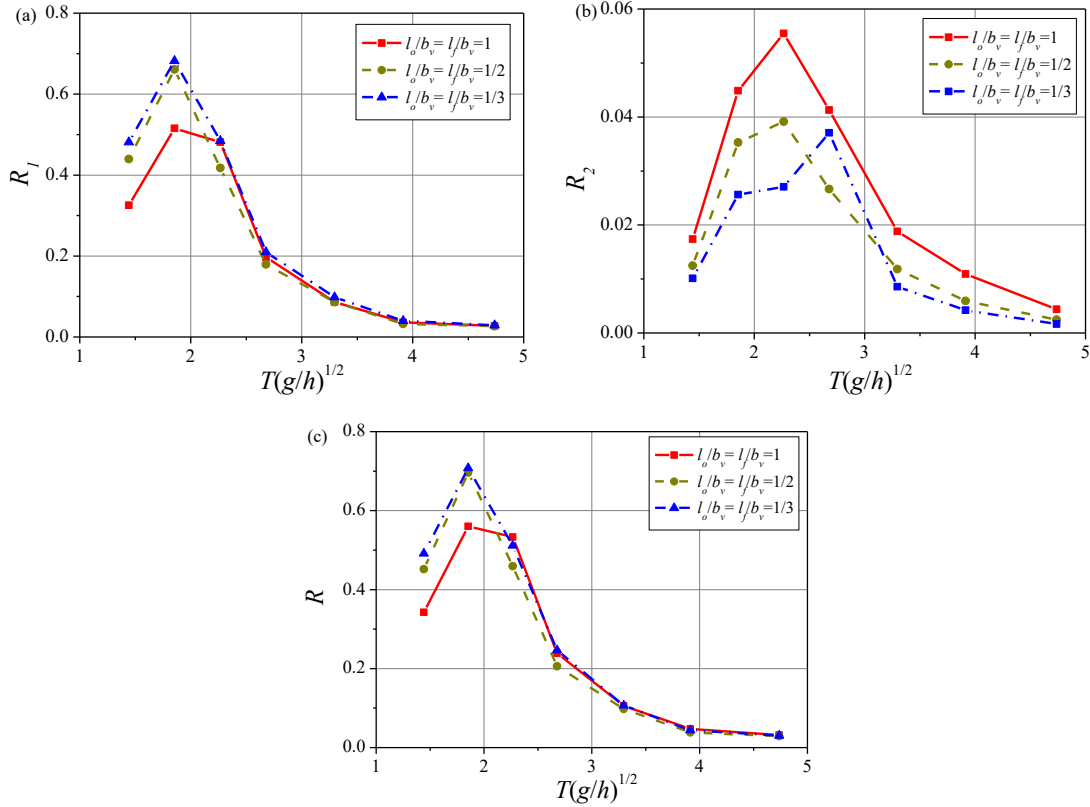

Fig. 13. Variations of energy conversion efficiency including (a) the OWCs R_1, (b) the OFs R_2 and (c) the total system R with dimensionless wave period $T(g/H_l)^{1/2}$ for different layouts
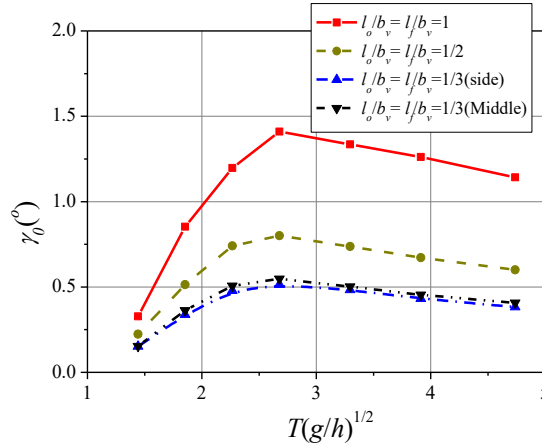

Fig. 14. Variations of rotational amplitude γ_0 of the OFs with dimensionless wave period $T(g/H_l)^{1/2}$ for different layouts

Fig. 15 presents the distribution of the hydroelastic response amplitude $w_0/(H_i/2)$ along the longitudinal centreline for $T(g/h)^{1/2}=1.8$ and 4.7, respectively. It can be found that the hydroelastic response is basically unchanged for different array layouts in short-period waves as shown in Fig. 15(a) but is reduced for more WECs in long-period waves as shown in Fig. 15(b). This can be explained from the point of view of the array effect: compared to the single OWC-OF device, array WECs can generate more higher-order waves with short wavelength due to multi-body hydrodynamic interation, strengthening wave energy absorption by the WEC devices. It can be

concluded that the hydroelastic reduction of the VLFS is insensitive to the number of WECs in short-period waves, while for long-period waves, an array of WECs consisting of two or more OWCs and OFs could be a better selection, to benefit more fully from the array effect, and in turn to improve the safety and serviceability of the VLFS efficiently.
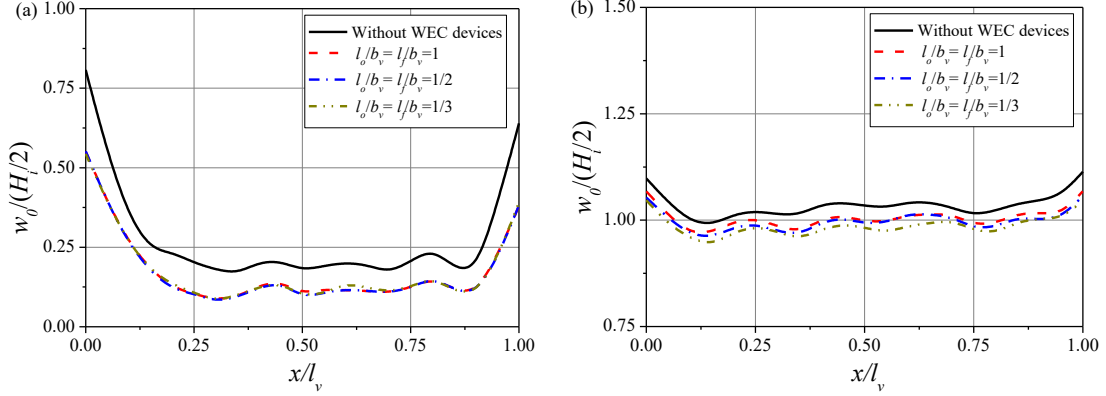

Fig. 15. Distributions of dimensionless vertical deflection amplitude $w_0/(H_I/2)$ along longitudinal centreline for (a) $T(g/h)^{1/2}=1.8$ and (b) $T(g/h)^{1/2}=4.7$

4.3 Effect of different WEC-VLFS gap distances

Three sets of gap distances between WECs and VLFS are considered(i.e. $b_g/h=0$, 0.14 and 0.27) for the VLFS integrated with two array OWC-OF WECs. The input parameters are kept the same with Section 4.2. Fig. 16(a)-(c) displays the variation of the energy conversion efficiency of the OWCs, the OFs and the overall integrated system, respectively. It can be seen from Fig. 16(a) that the conversion efficiency of the OWCs increases with increasing the WEC-VLFS gap distance in short-period waves but is insensitive in long-period waves. This is due to the fact that the relative gap distance b_f/λ is the determining factor for this problem. In short-period waves, the gap distance is not small relative to the incident wavelength, so that the waves can transmit into the gap and is reflected by the VLFS, leading the constrctive interference between transmitted and reflected waves. Conversely, in the long-period waves, the variation of the gap distance is small enough (i.e. $0.079<b_f/\lambda<0.16$ for $T(g/h)^{1/2}=3.3$ and $0.040<b_f/\lambda<0.08$ for $T(g/h)^{1/2}=4.7$) such that the variation of the wave period has weak influence on the conversion efficiency of the OWCs. The existence of the WEC-VLFS gap extends the effective frequency bandwidth of the OFs and enhance the maximum conversion efficiency by up to 1.15 times for $b_f/h=0.14$ and 1.25 times for $b_f/h=0.27$, as shown in Fig. 16(b). It is worth mentioning that the wave energy conversion is also improved in long-period waves by WEC-VLFS gap when the gap distance increases to $b_f/h=0.27$. This is because the scattering waves induced by the hydroelastic response of the VLFS focuses at the downstream of the OFs, boosting the rotational motion of the OFs. The overall efficiency curves in Fig. 16(c) further indicates the beneficial effect of the gap distance on the wave energy extraction.
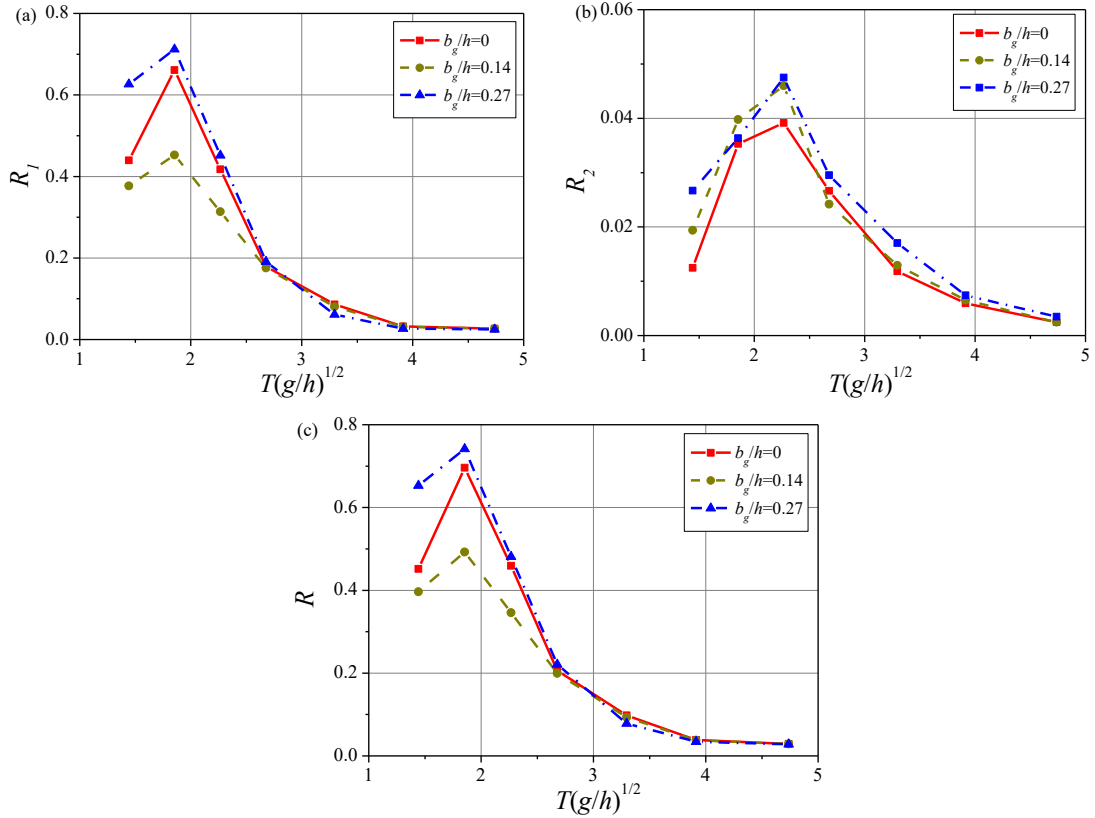
Fig. 16. Variations of energy conversion efficiency including (a) the OWCs R_1, (b) the OFs R_2 and (c) the total system R with dimensionless wave period $T(g/H_I)^{1/2}$ for different gap distances

Next, the distribution of the hydroelastic response amplitude $w_0/(H_i/2)$ of the VLFS along the longitudinal centerline is shown in Fig. 17(a) for $T(g/h)^{1/2}=1.4$ and Fig. 17(b) for $T(g/h)^{1/2}=4.7$. From Fig. 17(a), it can be obtained that the hydroelastic response of the VLFS increases with increasing WEC-VLFS gap distances, especially for the measured points closer to the incident waves. This is not surprising because the piston-type and sloshing-type motions of the water column in the WEC-VLFS gap mitigates the hydroelastic reduction efficiency of the facing-wave WECs. For long-period waves, i.e. $T(g/h)^{1/2}=4.7$ in Fig. 17(b), the gap (i.e. $b_f/h=0.14$) would worsen the hydroelastic performance at the back-end of the VLFS. In addition, the deflection degree of the VLFS is magnified by the gap distance. This is attributed to the fact that the scattering waves includes more higher-order components generated by the OF motion, and would increase wave loads on the bottom surface of the VLFS.
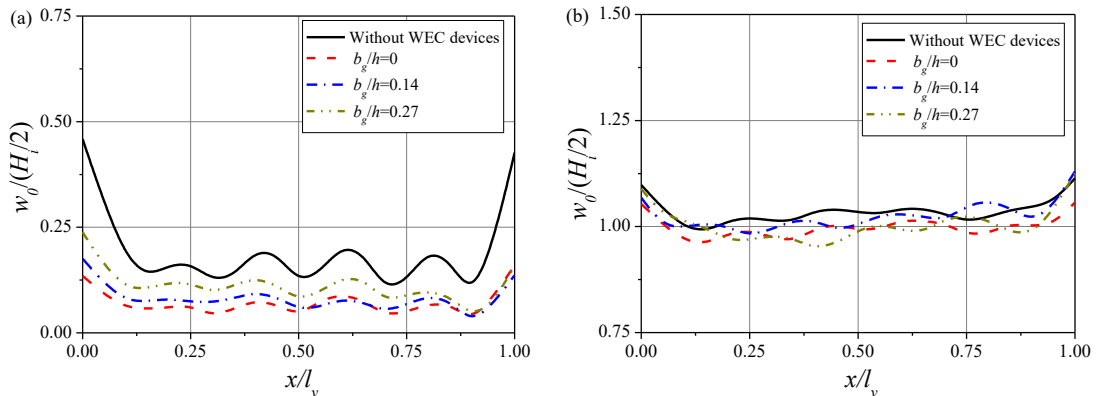
Fig. 17. Distributions of dimensionless vertical deflection amplitude $w_0/(H_I/2)$ along longitudinal centreline for (a) $T(g/h)^{1/2}$=1.4 and (b) $T(g/h)^{1/2}$=4.7

Fig. 18 plots the variation of the hydroelastic reduction at the fore-end of the VLFS with wave period. It can be seen that the hydroeasltic response increases as the WEC-VLFS distance b_f/h increases from 0 to 0.14 for most of wave periods, but decreases in the period region of 1.8< $T(g/h)^{1/2}$<3.9 as b_f/h increases from 0.14 to 0.27. This is because when the transmitted waves in the WEC-VLFS gap are in phase with the reflected waves by the VLFS, the amplified wave loads are generated. If the transmitted waves are out of phase with the reflected waves, the wave loads decrease. The alternating constructive and destructive interference of waves results in the oscillating vartiation of the hydroelastic reduction with wave period.
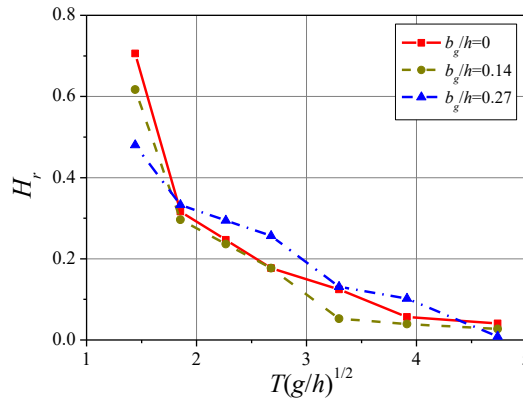

Fig. 18. Variations of hydroelastic reduction H_r with dimensionless wave period $T(g/H_I)^{1/2}$ for different gap distances

4.4 Effect of different chamber widths

All above solutions were obtained for a fixed chamber width. To further assess the effects of chamber width b_o/h, additional simulations for b_o/h=0.13 and 0.15 were also performed. The WEC-VLFS gap is set as b_g/h=0.0 and other parameters are kept the same with those in Fig. 18. Fig. 19 plots the variation of the energy conversion efficiency of the OWCs, the OFs and the overall integrated system with wave period, respectively. From Fig. 19(a), it can be seen that the energy conversion efficiency of the OWCs decreases with increasing the chamber width in short-period waves, and vice versa in long-period waves. This phenomenon can be explained that the water mass in the chamber increases with increasing the chamber width. Hence, short-period waves with a lower energy density can be more easily reflected by the water column, while long-period waves can propagate into the chamber, strengthening the piston-type motion of the water column. Similarly, the conversion efficiency of the OFs in long-period waves is also enhanced due to the volient motion of the internal water, as shown in Fig. 19(b). As shown in Fig. 19(c), the maximum energy conversion efficiency decreases with increasing the chamber width, with the maximum R=0.69, 0.65 and 0.63 respectively. The the maximum conversion efficiency occurs around period $T(g/h)^{1/2}$=1.8 which is almost unaffected by the chamber width.
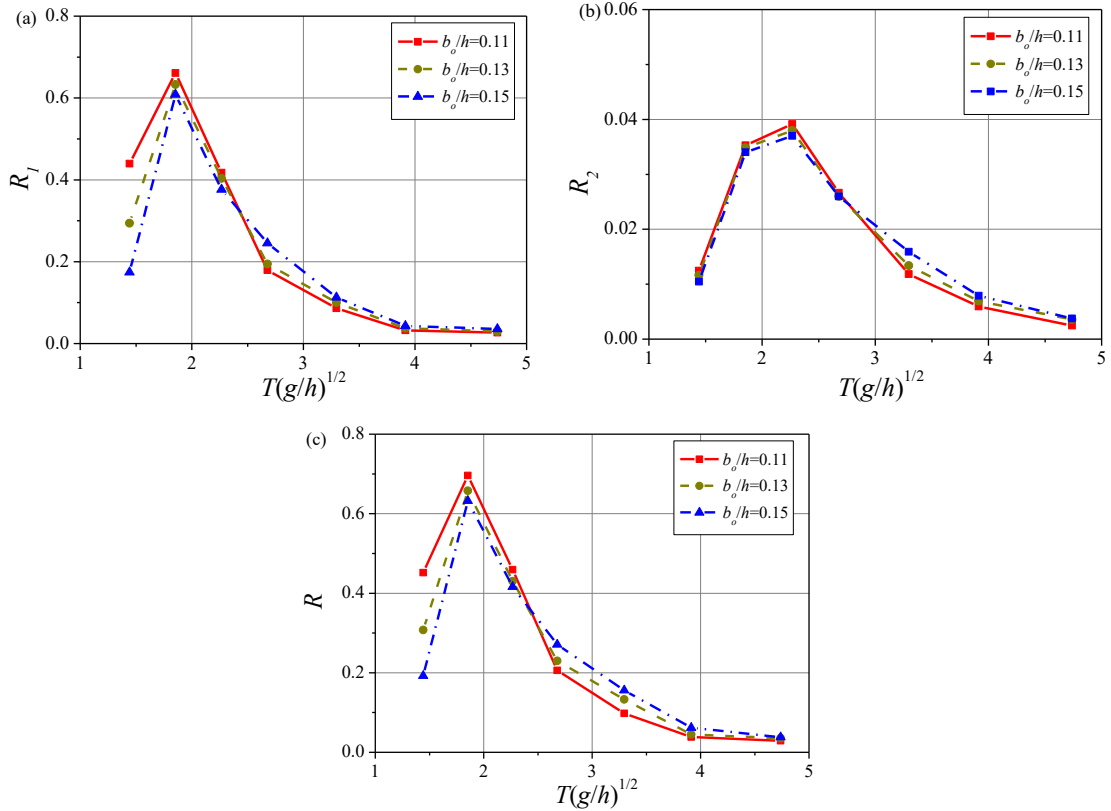
Fig. 19. Variations of energy conversion efficiency including (a) the OWCs R_1, (b) the OFs R_2 and (c) the total system R with dimensionless wave period $T(g/H_I)^{1/2}$ for different OWC widths

Fig. 20 depicts the distribution of the vertical deflection along the longitudinal centerline of the VLFS fo $T(g/h)^{1/2}$=1.4 and =4.7. From Fig. 20(a), it can be seen that the hydroelastic responses at fore-end location of the VLFS are almost same for different chamber widths in short-period waves, but the deflection degree at the interior locations are affected by the chamber width, especially for b_o/h=0.15. The similar phenomenon in long-period waves become more prominent for smaller chamber width i.e. b_o/h=0.13, as shown in Fig. 20(b). This is because some higher-order are generated in the chamber and are characterized by two different instrinsic ingredients i.e. free and locked waves. The percentage of the free and locked ingradients in higher-order waves varies with increasing chamber width. The free waves are released to cancel partly the transmission effect of waves but the locked waves are bounded in the transmitted waves to amplify wave loads.
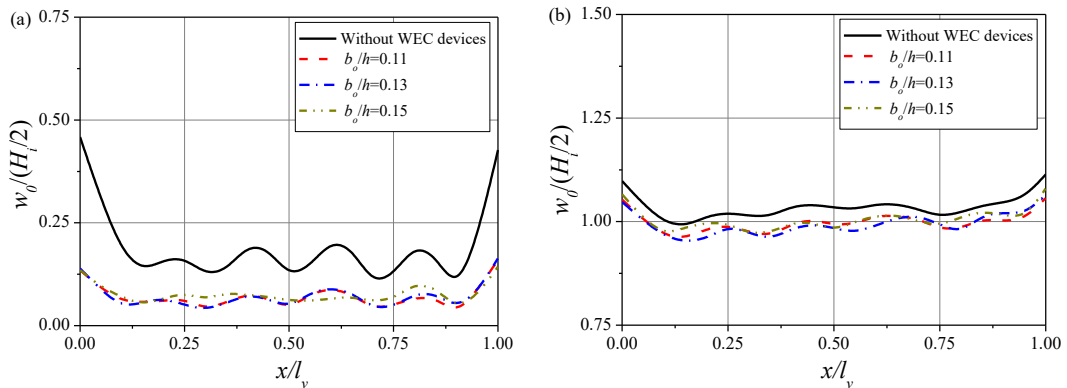

Fig. 20. Distributions of dimensionless vertical deflection amplitude $w_0/(H_I/2)$ along longitudinal centreline for (a) $T(g/h)^{1/2}$=1.4 and (b) $T(g/h)^{1/2}$=4.7

4.5 Effect of different OF heights

The effects of the submerged OF height d_f/h on the hydrodynamic performance of the WEC-VLFS integrated system are illustrated in this section. Fig. 21(a)-(c) presents the variation of the conversion efficiency of the OWCs, the OFs and the whole system with three different OF heights d_f/h=0.03, 0.048 and 0.065. The OWC chamber width b_o/h=0.11 is selected and other parameters are kept constant with Section 4.4. It can be seen from Fig. 21(a) that the energy conversion efficiency of the OWCs for the largest submerged depth d_f/h=0.065 is the largest in the wave period of $1.8 < T(g/h)^{1/2} < 3.3$ due to both the motion and the reflection of the OF enhancing the energy extraction ability of the OWCs, and and smallest in other wave periods. Fig. 21(b) indicates that the conversion efficiency of the OFs significantly increases with increasing OF height for all wave periods considered in this simulation. This is associated with that the PTO damping value of the OF in this case is appropriate for d_f/h=0.065 and large enough for d_f/h=0.003. Thus, as the OF height decreases to d_f/h=0.03, the motion velocity of the OF decreases rapidly and is close to be motionless, leading to lower the energy extraction according to the relative relationship between energy extaction and OF motion. The maximum conversion efficiency of the overall system is enchanced by 12.9% from the height d_f/h=0.03 to 0.048, but varies only 3% between d_f/h=0.048 and 0.065, as shown in Fig. 21(c). However, the effective frequency bandwidth decreases slightly with increasing OF height.
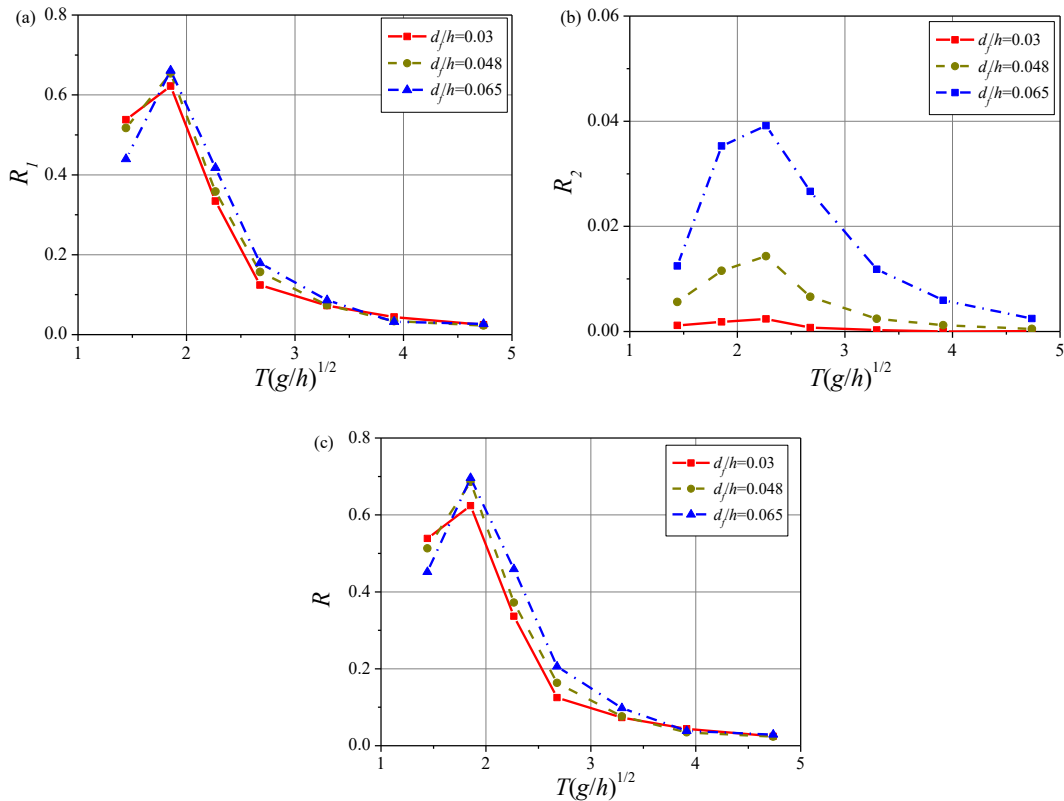

Fig. 21. Variations of energy conversion efficiency including (a) the OWCs R_1, (b) the OFs R_2 and (c) the total system R with dimensionless wave period $T(g/H_l)^{1/2}$ for different OF heights

Fig. 22(a) and (b) shows the distribution of the vertical deflection along the longitudinal centerline of the VLFS fo $T(g/h)^{1/2}$=1.4 and =4.7, respectively. From Fig. 22(a), it can be observed that the hydroelastic response at fore-end of the VLFS decreases with increasing the OF heights, but

is almost unchanged at the back-end of the VLFS for different OF heights. This is due to the fact that the fore-end of the VLFS is simultaneously subjected to the processing and scattering wave loads. As waves progagate from the fore-end to the back-end of the VLFS, the scattering waves gradually decay and only processing wave loads act on the back-end locations. Consequently, the scaterring wave loads decreases with increasing OF height in short-period waves. Fig. 22(b) reveals that the hydroelastic response of the VLFS is amplified at the location of $0.15 < x/l_v < 0.55$ with increasing the OF height in long-period waves, which is appears to be due to the scattering waves induced by the rotational motion of the OF.
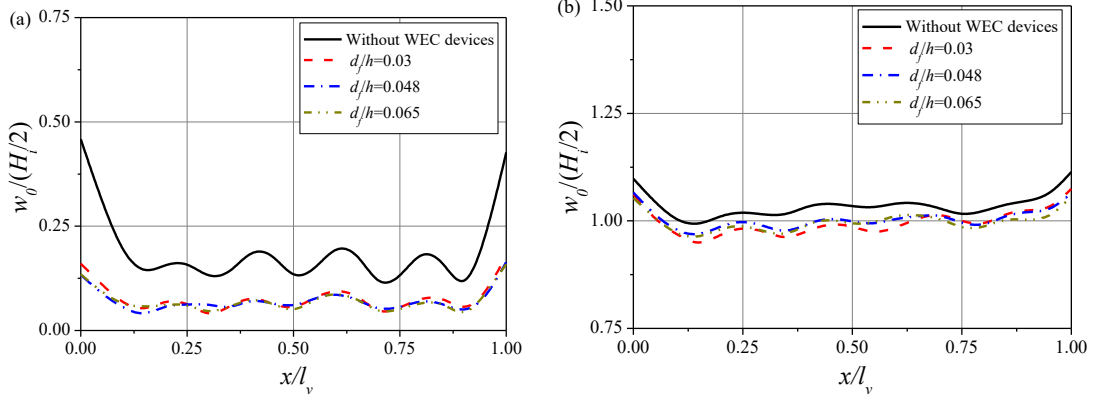

Fig. 22. Distributions of dimensionless vertical deflection amplitude $w_0/(H_I/2)$ along longitudinal centreline for (a) $T(g/h)^{1/2}=1.4$ and (b) $T(g/h)^{1/2}=4.7$

Fig. 23 plots the variation of the hydroelastic reduction of the VLFS with wave period for different OF heights. As the OF height increases, the hydroelastic response reduction is improved, especially around the resonant period of the water column in the chamber. This illustrates that a larger OF height can strength the water motion in the chamber, enhancing the energy exchange between transmitted waves and internal water column. The maximum improvement of the hydroelastic reduction is about 47.61% corresponding to the wave period $T(g/h)^{1/2}=1.8$ from $d_f/h=0.03$ to 0.065.
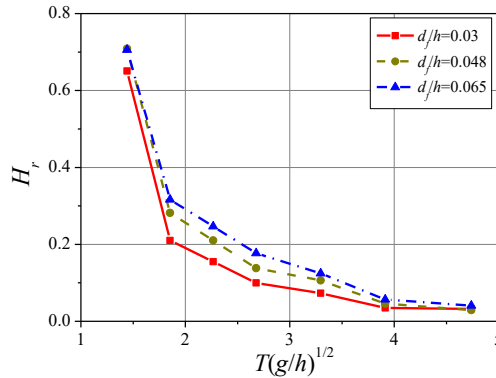

Fig. 23. Variations of hydroelastic reduction H_r with dimensionless wave period $T(g/H_I)^{1/2}$ for different OF heights

4.6 Effect of incident wave heights

The effects of wave height on the hydrodynamic performance of the OWC-OF-VLFS integration are examined in this section. The numerical simulations are performed with three different wave heights i.e. $H_i=0.02$ m, 0.06 m and 0.12 m. The WEC-VLFS gap distance is set as $b_g/h=0.14$ and other parameters are maintained the same with Section 4.3. Fig. 24(a)-(c) presents

the influence of wave height on the conversion efficiency of the OWCs, the OFs and the whole system versus wave period. It is clear from Fig. 24(a) that the conversion efficiency of the OWCs increases with increasing wave height in long-period waves, but increases firstly and then decreases with wave height in short-period waves. This is not surprising because that short-period waves with strong nonlinearity can generate more higher-order waves reflected by the front-chamber wall. The long-period waves with high transmission capacity can strengthen water motion in the chamber for strong nonlinearity. From Fig. 24(b), the reduction of the conversion efficiency of the OFs with wave height is observed in short-period waves. The wave periods corresponding to the maximum efficiency move toward larger periods for both OWC and OF devices. In Fig. 24(c), weaker wave nonlinearity i.e. H_i=0.06 m can enhance the maximum conversion efficiency of the overall system compared to H_i=0.02 m, but it is opposite for stronger wave nonlinearity i.e. H_i=0.12 m. This implies that a proper OWC-OF design should take into account the change of wave conditions which is important for the resonant characteristic and the operation efficiency, making it relatively rigorous to complete for practical applications.
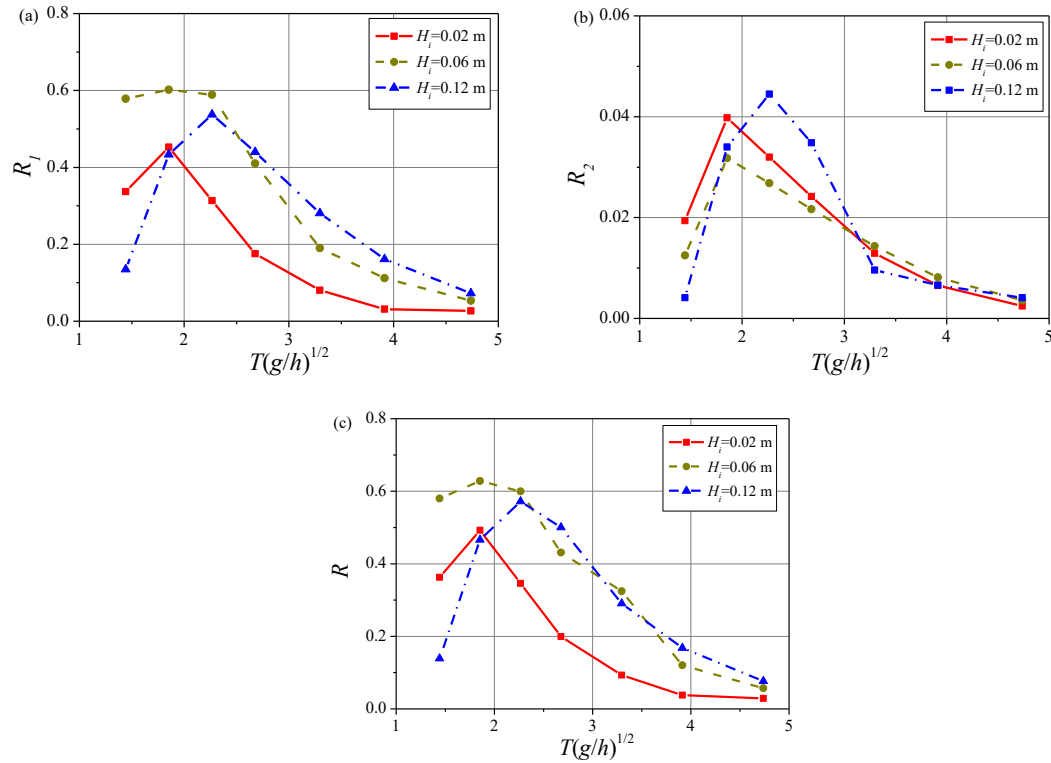

Fig. 24. Variations of energy conversion efficiency including (a) the OWCs R_1, (b) the OFs R_2 and (c) the total system R with dimensionless wave period $T(g/H_l)^{1/2}$ for different wave heights

Fig. 25(a) and (b) display the distribution of the vertical deflection along the longitudinal centerline of the VLFS fo $T(g/h)^{1/2}$=1.4 and =4.7, respectively. As shown in Fig. 25(a), in short-period waves, the hydroelastic response of the VLFS decreases with increasing wave height due to more wave energy reflection by the facing-wave WEC devices. In Fig. 25(b), at the initial stage of increasing wave height, the hydroelastic response of the VLFS diminishes due to more wave energy absorbed by WEC devices, which is coincide well with the wave energy exraction in Fig. 20. With further increasing wave height, the hydroelastic response increases at the interior locations and the back-end of the VLFS. This thanks to the multi-body interation between WECs and VLFS with multi-degree-of-freedom(MDOF) motions, achieving constructive interference of scattering waves.
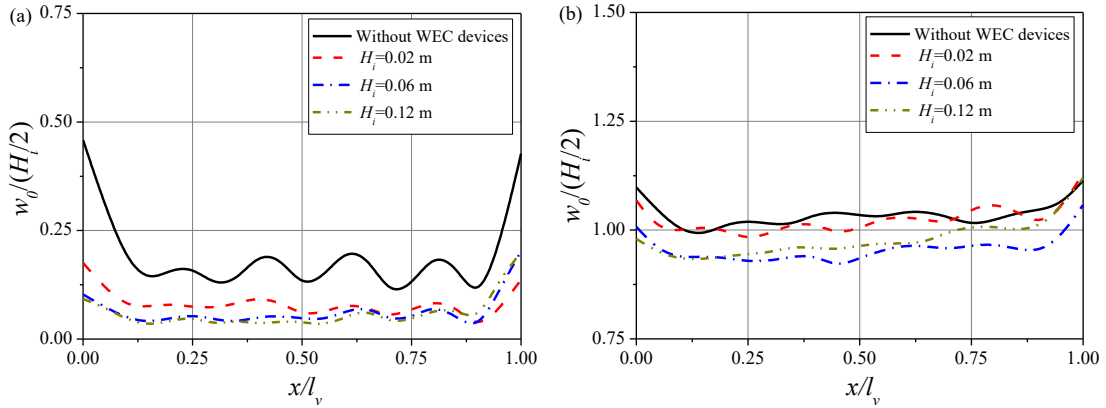
Fig. 25. Distributions of dimensionless vertical deflection amplitude $w_0/(H_I/2)$ along longitudinal centreline for (a) $T(g/h)^{1/2}=1.4$ and (b) $T(g/h)^{1/2}=4.7$

5. Conclusions

In this study, an array of WEC devices combining oscillating water columns (OWCs) and oscillating flaps (OFs) are considered to be integrated at the upstream from a pontoon-type VLFS. Each OF is hinged at the front/back-wall end of each OWC chamber, and thus there is an equal number of OWCs and OFs. Based on the time-domain modal expansion theory and the nonlinear potential flow theory, an accurate numerical model is developed to solve wave energy conversion and hydroelastic reduction problems of these WECs. The PTO systems for OWCs and OFs are represented by a quadratic pneumatic term into the water surface condition and a linear damping coefficient into the body motion equation, respectively. The application of the present numerical model is not restricted by the small wave steepness, and hence the coupled multi-body interaction and the influence of wave nonlinearity can be examined. After performing parametric sensitivity analysis, the following conclusions can be drawn.

(1) Comparisons between an OWC-OF-VLFS integration and a typical OWC-OF integration reveal that additional OFs play a constructive role in reducing the hydroelastic response of the VLFS. Additionally, the design of the OFs hinged at the back-wall end of the OWC chamber is preferred in terms of wave energy conversion due to more wave energy converged inside the chamber.

(2) A higher maximum energy conversion can be achieved by multiple OWCs and OFs compared to single OWC and OF due to the beneficial array effect, which in turn reduces the hydroelastic response of the VLFS, especially for long-period waves. The wave energy extraction of the OWCs outperforms that of the OFs for the periods near the main resonant periods of the WECs.

(3) A larger WEC-VLFS gap leads to the hydroelastic scattering waves generated by the VLFS motion more fully to interact with the WECs, enhancing both the maximum conversion efficiency and the effective frequency bandwidth. However, the vertical deflection of the VLFS increases with increasing gap distance in short-period waves due to the wave reflection by the leeside of WECs.

(4) Due to the fact that a wider chamber possesses greater internal water mass, the energy conversion efficiency decreases with chamber width in short-period waves and vice versa in long-period waves. The hydroelastic response at the interior locations of the VLFS is more sensitive to the width than that at fore-end of the VLFS.

(5) As the submerged height of OFs increases, a higher energy conversion efficiency and hydroelastic reduction are yielded across a broad frequency bandwith. This is associated with the

energy exchange between outside waves and inside water column.

(6) Wave nonlinearity has a strong effect on the maximum energy conversion efficiency as well as its corresponding period. For short-period waves with weaker nonlinearity, the overall energy conversion efficiency increases with wave height, and this opposite trend is observed for stronger wave nonlinearity.

The findings of this investigation are of importance and helps to enhance the design and the operational performance of WECs and VLFS integrated system. The developed numerical model can be used to simulate extreme waves interacting with such integrated systems. Further work will focus on the optimized configuration of WEC-VLFS integration in multi-directional irregular waves which are more realistic wave conditions.

CRediT authorship contribution statement

Yong Cheng: Methodology, Software, Data curation, Writing-original draft, Supervision. **Fukai Song:** Validation, Formal analysis, Writing-original draft, Investigation. **Chen Xi:** Validation, Writing-review & editing. **Maurizio Collu:** Writing-review & editing, Supervision. **Zhiming Yuan:** Writing-review &editing. **Atilla Incecik:** Supervision.

Declaration of Competing Interest

The authors declare that they have no known competing financial interests or personal relationships that could have appeared to influence the work reported in this paper.

Acknowledgment

References

[1] International Energy Agency (IEA). Renewables 2020 Data Explorer: 2020-data- explorer ? mode= market&region=World&product=Total,2020.

[2] Goel S, Sharma R. Peformance evaluation of stand alone, grid connected and hybrid renewable energy systems for rural application: A comparative review. Renew Sust Energy Rev 2017;78:1378-1389.

[3] Jin S, Greaves D. Wave energy in the UK: Status review and future perspectives. Renew Sustain Energy Rev 2021;143:110932.

[4] Smart G, Noonan M. Tidal stream and wave energy cost reduction and industrial benefit. ORE Catapult Glasgow; 2018, https://periscope-network.eu/analyst/tidal-stream-and-wave-energy-cost-reduction-and-industrial-benefit [Accessed on 10/11/2021].

[5] Falcão AFO, Henriques JCC. Oscillating-water-column wave energy converters and air turbines: a review. Renew Energy 2016;85:1391-1424.

[6] Evans DV. The oscillating water column wave energy device. IMA J Appl Math 1978;22(4):423-433.

[7] Sarmento AJNA, Falcão AFO. Wave generation by an oscillating surface-pressure and its application in wave-energy extraction. J Fluid Mech 1985;150:467-485.

[8] Ning DZ, Zhou Y, Zhang CW. Hydrodynamic modelling of a novel dual-chamber OWC wave energy converter. Appl Ocean Res 2018;78:180-191.

[9] Ning DZ, Zhou Y, Mayon R, Johanning L. Experimental investigation on the hydrodynamic performance of a cylindrical dual-chamber Oscillating Water Column device. Appl Energy 2020;260:114252.

[10] Elhanafi A, Macfarlane G, Ning D. Hydrodynamic performance of single-chamber and dual-chamber offshore-

stationary Oscillating Water Column devices using CFD. Appl Energy 2018;228:82-96.

[11] He F, Huang ZH, Adrian WKL. An experimental study of a floating breakwater with asymmetric pneumatic chambers for wave energy extraction. Appl Energy 2013;106:222-231.

[12] He F, Leng J, Zhao XZ. An experimental investigation into the wave power extraction of a floating box-type breakwater with dual pneumatic chambers. Appl Ocean Res 2017;67:21-30.

[13] Zhao XL, Zhang LD, Li MW, Johanning L. Experimental investigation on the hydrodynamic performance of a multi-chamber OWC-breakwater. Renew Sust Energy 2021;150:111512.

[14] Shalby M, Dorrell DG, Walker P. Multi-chamber oscillating water column wave energy converters and air turbines: A review. Int J Energy Res 2018:1-16.

[15] Howe D, Nader JR, Macfarlane G. Experimental investigation of multiple oscillating water column wave energy converters integrated in a floating breakwater: energy extraction performance. Appl Ocean Res 2020;97: 102086.

[16] Howe D, Nader JR, Macfarlane G. Experimental investigation of multiple oscillating water column wave energy converters integrated in a floating breakwater: energy extraction performance. Appl. Ocean Res 2020;99, 102160.

[17] Zheng SM, Antonini A, Zhang YL, Greaves D, Miles J, Iglesias G. Wave power extraction from multiple oscillating water columns along a straight coast. J Fluid Mech 2019;878:445-480.

[18] Doyle S, Aggidis GA. Experimental investigation and performance comparison of a 1 single OWC, array and M-OWC. Renew Energy 2021;168:365-374.

[19] Hang MM, Wang CM. Coupled analytical-numerical approach for determining hydrodynamic response of breakwater with multiple OWCs. Mar Struct 2021;80:103097.

[20] Zheng SM, Zhang YL. Theoretical modelling of a new hybrid wave energy converter in regular waves. Renew Energy 2018;128:125-141.

[21] Cui L, Zheng SM, Zhang YL, Miles J, Iglesias G. Wave power extraction from a hybrid oscillating water column-oscillating buoy wave energy converter. Renew Sustain Energy Rev 2021;135:110234.

[22] Wang C, Zhang YL, Deng ZZ. Semi-analytical study on the wave power extraction of a bottom-seated oscillating water column device with a pitching front lip-wall. J Fluid Struct 2021;105:103350.

[23] Mustapa MA, Yaakob OB, Ahmed YM, Rheem CK, Koh KK, Adnan FA. Wave energy device and breakwater integration: A review. Renew Sust Energy Rev 2017;77:43-58.

[24] Nguyen HP, Wang CM, Luong VH. Two-mode WEC-type attachment for wave energy extraction and reduction of hydroelastic response of pontoon-type VLFS. Ocean Eng 2020;197:106875.

[25] Nguyen and Wang. Heaving wave energy converter-type attachments to a pontoon-type very large floating structure. Eng Struct 2020;219:110964.

[26] Zhang HC, Xu DL, Zhao H, Xia S, Wu YS. Energy extraction of wave energy converters embedded in a very large modularized floating platform. Energy 2018;158:317-329.

[27] Zhang HC, Xu DL, Ding R, Zhao H, Lu Y, Wu YS. Embedded power take-off in hinged modularized floating platform for wave energy harvesting and pitch motion suppression. Renew Energy 2019;25:1176-1188.

[28] Zhang XT, Lu D. An extension of a discrete-module-beam-bending-based hydroelasticity method for a flexible structure with complex geometric features. Ocean Eng 2018;163:22-28.

[29] Tay ZY. Performance and wave impact of an integrated multi-raft wave energy converter with floating breakwater for tropical climate. Ocean Eng 2020;218:108136.

[30] Crema I. Oscillating water column wave energy converters integrated in very large floating structures. PhD thesis University of Florence 2017.

[31] Float Inc. Float Inc.: floating Shipping platform and wave energy production. http://maribe.eu/wp-

content/uploads/2016/10/b-1-float-inc-final-report.pdf [Accessed on 1/11/2019].

[32] Sheng S, Wang K, Lin H, Zhang Y, You Y, Wang Z, Chen A, Jiang J, Wang W, Ye Y. Model research and open sea tests of 100kW wave energy convertor Sharp Eagle Wanshan. Renew Energy 2017;113:587-595.

[33] Cheng Y, Xi Chen, Dai SS, Ji CY, Collu M, Li MX, Yuan ZM, Incecik A. Wave energy extraction and hydroelastic response reduction of modular floating breakwaters as array wave energy converters integrated into a very large floating structure. Appl Energy 2022;306:117953.

[34] Fenton JD. A fifth order Stokes theory for steady waves. J Waterw Port Coast Ocean Eng ASCE 1985; 111: 216-234.

[35] Mei CC, Stiassnie M, Yue DKP. Theory and applications of ocean surface waves. World Scientific Publishing Co Pte Ltd 2005.

[36] Wei Y, Abadie T, Henry A, Dias F. Wave interaction with an oscillating wave surge converter, Part II: Slamming. Ocean Eng 2016;113:319-334.

[37] Wang YZ, Liu ZQ. Proposal of novel analytical wake model and GPU-accelerated array optimization method for oscillating wave surge energy converter. Renew Energy 2021;179:563-583.

[38] Yago K, Endo H. On the hydroelastic response of box-shaped floating structure with shallow draft. J Soc Nav Archit Japan 1996;180:341-352.